Catalytic and thermal decomposition of ionic liquid monopropellants using a dynamic reactor
Comparison of powder and sphere-shaped catalysts

Dan Amariei, Laurence Courthéoux, Sylvie Rossignol *, Charles Kappenstein

University of Poitiers, LACCO UMR CNRS 6503, Laboratoire de Catalyse par les Métaux, 40 Avenue du Recteur Pineau, F-86022 Poitiers Cedex, France
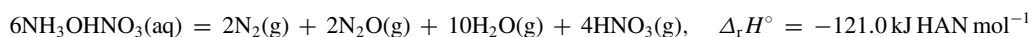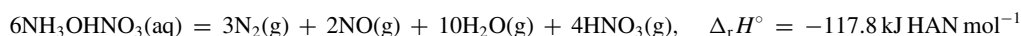
Abstract

A dynamic reactor with mass spectroscopy online product analysis has been used to study the thermal and catalytic decompositions of ionic liquid HAN-based monopropellants. The activity of different catalysts has been evaluated by determining qualitatively and quantitatively the reaction products. A careful calibration of the expected products detected by the mass spectrometer (MS) (N_2, O_2, N_2O, NO and NO_2) has been performed. The analytical results have been supplemented by Raman spectroscopy of the aqueous solutions trapped after the reactor.

The thermal and catalytic decomposition of water–HAN (80 wt.%, hydroxylammonium nitrate $NH_3OH^+NO_3^-$) mixture gave primary products (major N_2, medium NO) and secondary products (medium N_2O and traces NO_2). From the data, a reaction mass balance could be proposed, based on the combination of two parallel competitive reactions:

$$6NH_3OHNO_3(aq) = 3N_2(g) + 2NO(g) + 10H_2O(g) + 4HNO_3(g), \quad \Delta_r H^\circ = -117.8\,kJ\,HAN\,mol^{-1}$$

$$6NH_3OHNO_3(aq) = 2N_2(g) + 2N_2O(g) + 10H_2O(g) + 4HNO_3(g), \quad \Delta_r H^\circ = -121.0\,kJ\,HAN\,mol^{-1}$$

The influence of the catalyst shape (powder or spheres) has been followed. The isothermal tests at 50 °C display the best activity for the powder catalyst with a complete decomposition of the HAN solution, due to a good contact between catalyst bed and monopropellant. On the other hand, the sphere-shaped catalyst leads only to a partial HAN decomposition, due to preferential paths through the catalyst bed. The thermal decomposition at 200 °C, leads also to a partial reaction.
© 2006 Elsevier B.V. All rights reserved.

Keywords: Pt/SiAl$_2$O$_3$; Online analysis; Dynamic reactor; Monopropellant

1. Introduction

The study and development of new monopropellants as hydrazine substitutes for propulsion applications are currently investigated to reduce handling and storage costs and to increase engine performance [1]. The most cited merit of these new propellants is their reduced toxicity and keywords like '*non-toxic propellants*' or '*green propellants*' are extensively used in literature and proceedings [2]. In previous papers, describing the replacement of hydrazine by hydrogen peroxide or by HAN-based ionic liquid monopropellants (HAN: hydroxylammonium nitrate $NH_3OH^+NO_3^-$), we have presented the design and use of a very versatile, constant volume, laboratory batch reactor [3,4], and preliminary results on the catalytic decomposition of binary HAN–water mixtures [5]. These results have shown that platinum supported on silica-doped alumina catalysts (Pt/Al$_2$O$_3$-Si) are able to trigger the decomposition of a HAN–water solution (80 wt.% HAN) at low temperature and remain active in solution after 15 or more injections of HAN [6–8]. However, the experimental pressure increase remains lower than the pressure calculated on the basis of the formation of the sole thermodynamic products, i.e. nitrogen, oxygen and water. This discrepancy is due to the formation of nitrogen oxides (N_2O, NO and NO_2) as kinetic products and to the aqueous solubility of NO_2. As the kinetic product formation decreases the engine performance, the assessment of the

* Corresponding author. Tel.: +33 549 454157; fax: +33 549 454020.
E-mail address: sylvie.rossignol@univ-poitiers.fr (S. Rossignol).

parameters governing the final reaction products is a critical part of our study.

Therefore, the objective of the current study is to determine qualitatively and quantitatively, the products formed during thermal and catalytic decompositions of energetic ionic liquids; from these data, we can establish the reaction mass balance we need to calculate the propulsion performances. For this purpose, we have designed and developed a dynamic reactor with online analysis of the decomposition products by means of a mass spectrometer (MS); this reactor has been described in a previous paper [9]. It enables us to evaluate the catalytic activity and the selectivity of the monopropellant decomposition at atmospheric pressure under a neutral gas flow. The results presented here have been supplemented by a careful calibration of the mass spectrometer for the different reaction products. The MS data associated with the characterization of the condensates by Raman spectroscopy allowed us to propose a mass balance of the products. New results obtained on powder and sphere-shaped catalysts are presented and discussed to investigate the effect of the shape forming.

2. Experimental

2.1. Dynamic reactor

2.1.1. Design of the reactor

The reactor is a fixed bed reactor with online mass-spectrometer analysis of the gaseous decomposition products (Fig. 1); it is a modified version of the previous reactor [9]. The catalytic tests are performed under helium flow and the monopropellant is injected manually through a septum using a microsyringe. The design of this apparatus avoids the propellant flowing on the reactor wall surface before reaching the catalyst bed. The powder or sphere-shaped catalyst (160 mg) is put into a quartz reactor (internal diameter: 13 mm, catalyst bed height: 2 mm) and can be heated with a fixed slope (2–10 K min^{-1}) or preheated at a defined temperature (20–300 °C). Excess water

is condensed in a trap situated just below the reactor and kept at 0 °C; a downstream tube filled with silica gel eliminates the rest of the water in the gas flow.

Decomposition products are analyzed by means of a mass spectrometer (Pfeiffer; Model Omnistar; m/z range 0–200; quadrupole QME200). The analyses are performed using the Quadstarr 422 software with an ionization voltage of 70 eV and an emission current of 1 mA; the intensity of the ionic current is recorded versus time. The mass spectrometer calibration is achieved using a specifically designed device (Fig. 2) to inject controlled mixtures of the expected nitrogen oxides diluted in argon (NO$_2$ 4.58 ± 0.23 vol.%; NO 5.02 ± 0.10 vol.%; N$_2$O 5.13 ± 0.10 vol.%) and pure gases O$_2$, N$_2$, purchased from Air Liquide Company, France.

2.1.2. Decomposition products

HAN–water binary mixture containing 80 wt.% HAN has been used. The thermodynamic decomposition products are water, nitrogen and oxygen (Table 1, Eq. (1)), whereas several kinetic products (NO, NO$_2$, N$_2$O, HNO$_3$) have been identified corresponding to various reactions (Eqs. (2)–(7)) [10–13]. Table 1 gathers different reaction equations sorted by increasing reaction enthalpies ($\Delta_r H^\circ$). For the thermodynamic calculations, we used HSC software [14] and we took -344 kJ mol^{-1} as formation enthalpy of aqueous HAN. From these data, several products can be expected that do not disfavor too much the energetic balance of the reaction by comparison with the thermodynamic products. For each species, relative intensities of the mass spectrum peaks are given in Table 2; they are taken from the NIST WebBook databases [15] and correspond to ionization energy of 70 eV; no data could be found for the species HNO, HNO$_2$ and HNO$_3$. The peak at m/z 30 is due to the contribution of three species, namely NO (main peak), NO$_2$ (main peak) and N$_2$O (second peak); to discriminate between these species, we used the second peak at m/z 46 for NO$_2$ and the main peak at m/z 44 for N$_2$O (Table 2). This procedure requires a calibration of the mass spectrometer in order to quantify the contribution of
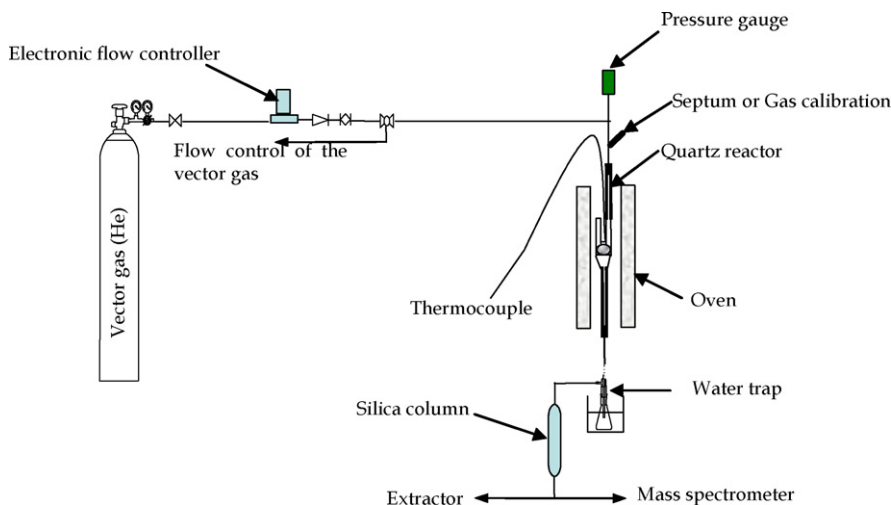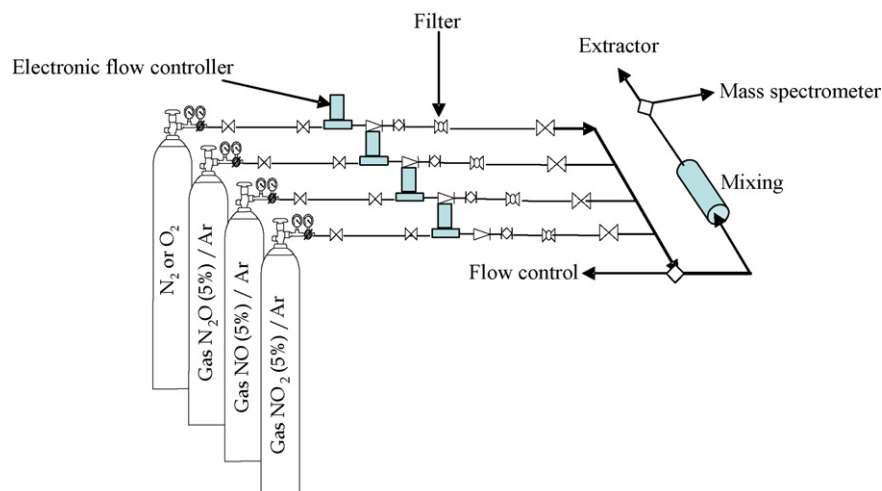

Fig. 1. Design of the dynamic reactor.

Fig. 2. Design of the gas calibration apparatus used for the mass spectrometer.

Table 1
Balanced equations for different HAN decomposition schemes and corresponding reaction enthalpy

Balanced equation		$\Delta_r H°$ (298) (kJ mol^{-1})
$[NH_3OH]^+[NO_3]^-(aq) = 2H_2O(g) + N_2(g) + O_2(g)$	(1)	−139.7
$[NH_3OH]^+[NO_3]^-(aq) = 2H_2O(g) + 0.5N_2(g) + NO_2(g)$	(2)	−105.5
$[NH_3OH]^+[NO_3]^-(aq) = 0.75N_2O(g) + 0.5HNO_3(g) + 1.75H_2O(g)$	(3)	−85.0
$[NH_3OH]^+[NO_3]^-(aq) = 0.8N_2O(g) + 0.4HNO_3(g) + 1.8H_2O(g) + 0.1O_2(g)$	(4)	−79.6
$[NH_3OH]^+[NO_3]^-(aq) = 2H_2O(g) + N_2O(g) + 0.5O_2(g)$	(5)	−58.1
$[NH_3OH]^+[NO_3]^-(aq) = 2H_2O(g) + 2NO(g)$	(6)	+42.9
$[NH_3OH]^+[NO_3]^-(aq) = NH_2OH(g) + HNO_3(g)$	(7)	+160.1

All the products are taken in gaseous phase.

each gas for each m/z value. Moreover, nitric acid, nitrous acid and nitrogen dioxide are dissolved in the water trap leading to an incomplete mass balance of these species.

2.1.3. Experimental conditions

Two studies were carried out: a thermal decomposition and a catalytic decomposition of HAN–water mixture. Whatever the reaction (thermal or catalytic decomposition), 100 µL of HAN solution was injected using a micro-syringe, under helium flow (about 165 mL min^{-1}). The thermal decomposition was obtained for a bed temperature of 200 °C. For the catalytic decomposition, 160 mg of catalyst have been put into the reactor and two heating procedures were used: temperature increase mode (7 K min^{-1}) and isothermal mode (50 or 85 °C). The inten-

sity of the mass spectrum peaks are collected, for every mass between 0 and 100, for 50 ms per m/z unit.

2.2. Catalyst and propellant

2.2.1. Catalyst

The catalyst (Pt/Al$_2$O$_3$Si) has been described in previous evaluation tests [16]. Si doped alumina supports were synthesized through sol–gel procedure using aluminum trisecbutoxide (Al(O-CH(CH$_3$)-C$_2$H$_5$)$_3$) as precursor and silicon tetraethoxide (Si(O-C$_2$H$_5$)$_4$) to introduce Si as doping element [17]. The resulting boehmite wet gel was dried under subcritical conditions (oven, 120 °C, 12 h, air flow) to form xerogel samples which were subsequently calcined at 1200 °C. A shape

Table 2
Relative intensity of the different mass spectrum peaks for the various gaseous products [14]

	4	14	15	16	17	18	20	28	30	32	40	44	45	46
He	100													
H$_2$O				0.9	21.1	100								
N$_2$		5.2						100						
NO		7.5	2.4	1.5					100					
O$_2$				22						100				
Ar							14.5				100			
N$_2$O		12.9		5				10.8	31.1			100	0.7	
NO$_2$		9.6		22.3					100					37

designed sample was realized from xerogel powder by CTI Company (Céramiques Techniques et Industrielles, 38000 Salindres, France) and named "spheres" in order to develop the catalyst for industrial applications. The platinum active phase was introduced onto the surface of the calcined support through two or three wetness impregnation procedures, using an aqueous solution of hexachloroplatinic acid H_2PtCl_6. After drying at $120\,°C$, H_2-reduction at $400\,°C$ leads to the formation of medium platinum crystallites (17–21 nm). The catalysts are named, respectively $5(i+i)Pt$ (powder, two impregnations) and $3(i+i+i)Pt$ (spheres, three impregnations). The average size of the powder particles is $50\,\mu m$; the average diameter of the spheres is about 1.5 mm.

2.2.2. Monopropellant preparation

HAN–H_2O mixture was prepared by controlled reaction (Eq. (8)) between concentrated aqueous solution of hydroxylamine (50 wt.%) and nitric acid (65–70 wt.%), both of high purity (Aldrich Company).

$$NH_2OH(aq) + HNO_3(aq) \rightarrow [NH_3OH]^+[NO_3]^-(aq) \qquad (8)$$
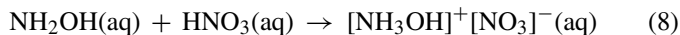
The temperature is continuously kept under $4\,°C$ and the end of the acid–base reaction is detected by a pH comprise between 3 and 2.5. The resulting ionic solution contains approximately 60 wt.% HAN and is concentrated using a rotating evaporator, to reach the expected concentration of about 80 wt.%. The 80 wt.% HAN content is checked by density measurements at $25\,°C$ ($1.51\,g\,cm^{-3}$) using the following formula (Eq. (9)) where $w(HAN)$ represents the HAN mass fraction [18]:

$$\rho = \frac{107.85}{96.042 - w(HAN) \times 30.99} \qquad (9)$$

The water content is further controlled by thermal analysis measurements to determine the evaporated water percentage [2].

3. Results

3.1. Mass spectrometer calibration

Several gaseous mixtures containing O_2, N_2, NO, N_2O and NO_2 in argon and helium flows, have been analyzed by mass spectrometry to establish the calibration plots; Table 3 displays typical compositions and peak intensities for some of the mixtures. Fig. 3 shows the mass spectrum results for the ternary mixture containing the three nitrogen oxides (Table 3, last row). For pure N_2 and O_2, the gas percentage can be extended to 30 vol.%, whereas for the nitrogen oxides, the dilution of these gases in argon limits the percentage from 0.1 to 2.4 vol.%. During HAN decomposition, the experimental values are generally inside this percentage and then could be easily interpolated. The relative intensities of each gas was corrected, taking into account the vector gas (helium) as internal standard. From all these experiments, a calibration curve is established for each gas and presented in Fig. 4. The plot of the intensity, as a function of the gas rate, is clearly linear. For NO gas, the scattered distribution of the experimental points around the linear plot is due to

Table 3
Calibration of the mass spectrometer.

Relative intensity		Mass (*m/z*)									Ratio
Gas	%	4	28	30			32	40	44	46	
		He (100)	N_2 (100)	NO (100)	NO_2 (100)	N_2O (31)	O_2 (100)	Ar (100)	N_2O (100)	NO_2 (37)	
Intensity (10^{-9} A)											
O_2	1.14						13.6				
Ar	37.99							251			
He	60.87	210									
N_2	1.17		16.8								
Ar	37.98							258			
He	60.85	216									
NO	1.93			24							
Ar	36.43							245			
He	61.64	284									
N_2O	2.01					3.29			14.0		**4.26**
Ar	37.18							250			
He	60.81	251									
NO_2	1.46				5.69					2.70	**2.11**
Ar	30.48							222			
He	68.06	276									
NO	0.66			**8.60**							
NO_2	0.18				**0.99**					0.47	**2.11**
N_2O	1.00					**1.61**			6.83		**4.26**
Ar	34.74							239			
He	63.42	255									

Peak intensity for nitrogen, oxygen and nitrogen oxides diluted in argon and helium. The relative intensities, taken from the NIST database [14], are given in parenthesis (bold values are calculated from ratio).
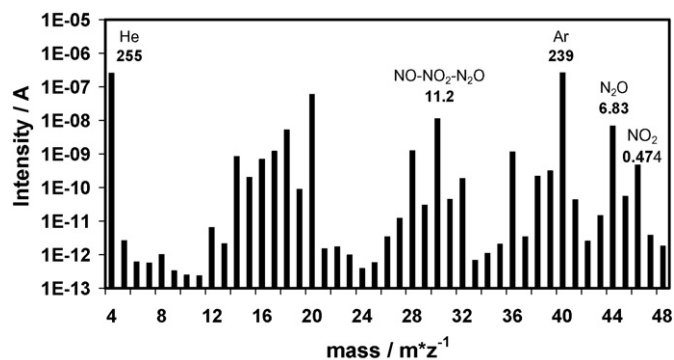
Fig. 3. Peak intensity vs. m/z measured from a ternary NO, N_2O and NO_2 mixture (the intensity number given in the figure is multiplied by 10^9).

the fact that the intensities plotted are not directly measured but calculated by subtracting the N_2O and NO_2 contributions at m/z 30. Concerning the N_2O and NO_2 calibration curves, the plotted intensities are respectively taken from m/z values of 44 and 46.

Then, by calculating the slope of the different calibration curves using a linear fit (Table 4), it is possible to determine the percentage of each gas in the product mixture from experimental intensities (corrected from helium standard).
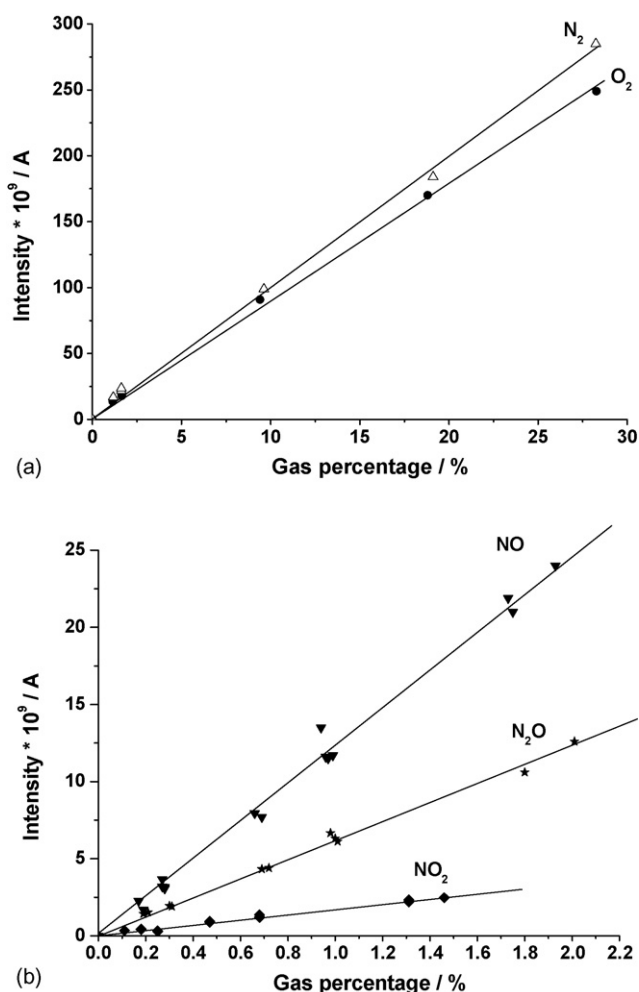

(a)

(b)

Fig. 4. Calibration plots of the expected gas: (a) N_2, O_2 and (b) NO, NO_2, N_2O.

Table 4
Slope values issued from gas calibration using a linear fit

Gas	Slope value	Standard deviation	Correlation coefficient	Number of data points
N_2	9.993E−9	1.53E−10	0.999	7
O_2	8.948E−9	1.18E−10	0.999	7
N_2O	6.195E−9	8.19E−11	0.998	12
NO	1.234E−8	1.69E−10	0.997	16
NO_2	1.755E−9	3.85E−11	0.993	14

3.2. HAN solution decomposition

3.2.1. Analysis of the trapped products by Raman spectroscopy

After the decomposition reaction, water excess is condensed in the cold trap and dissolves a part of the reaction products. The collected liquids, obtained after the catalytic tests at 50 and 85 °C, have been analyzed by Raman spectroscopy. For comparison purposes, $HAN_{80\%}$–water mixture and nitric acid (65 and 10 wt.%) have been also analyzed. The Raman spectra are presented in Fig. 5 and the corresponding vibration bands are gathered and assigned in Table 5 [19,20]. All the Raman bands of concentrated nitric acid solution (65 wt.%) are attributed to molecular HNO_3 species (strong bands at 688, 955 and 1304 cm^{-1}, Fig. 5f) and nitrate ions (strong band at 1040 cm^{-1}). On the contrary, the Raman spectrum of more diluted nitric acid solution (10 wt.%) shows a strong intensity decrease of bands corresponding to molecular nitric acid, whereas the nitrate band displays a slight increase (Fig. 5e); this suggests, as expected, an important ionization at this concentration for aqueous nitric acid, as established by Minogue et al. [19]. The Raman spectrum of the $HAN_{80\%}$–water solution presents only
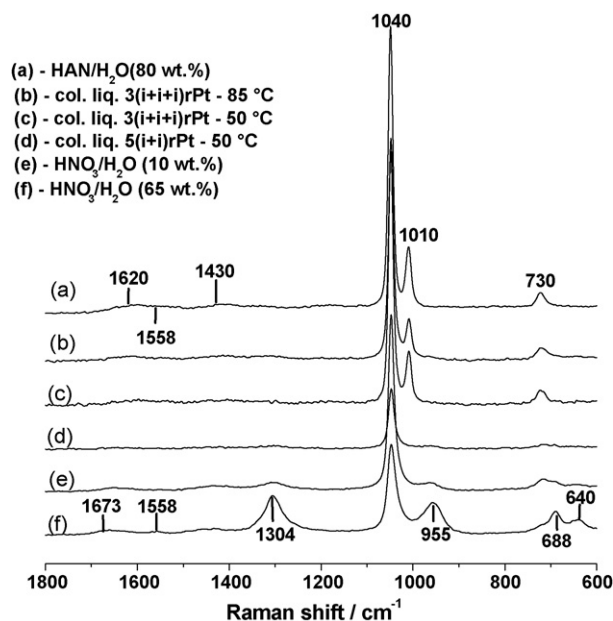

Fig. 5. Raman spectra of $HAN_{80\%}$–water mixture, collected liquids after isothermal tests at 50 and 85 °C with powder and pellet catalysts and HNO_3 aqueous solutions (10 and 65 wt.%).

Table 5
Frequencies of Raman active vibration modes for species present in HAN solutions (s: strong, m: medium, w: weak) [18,19]

Entity	Wave number (cm^{-1})	Vibration mode
Nitric acid (HONO$_2$)		
O—N—O$_{(rock)}$	640 (m)	δ/rock
O—N—O	688 (m)	δ/scissors
N—(OH)	955 (s)	ν
NO$_2$	1304 (s)	ν_s
Out-of-plane	1558 (w)	$2 \times \delta$
NO$_2$	1673 (w)	ν_{as}
Nitrate ion (NO$_3^-$)		
NO$_3^-$	730 (m)	δ
NO$_3^-$	1040 (s)	ν_{1s}
NO$_3^-$	1430 (w)	ν_{3as}
Out-of-plane	1558 (w)	$2 \times \delta$
Hydroxylammonium ion (NH$_3$OH$^+$)		
N—OH	1010 (s)	ν_{as}
OH/NH$_3$	1040 (s)	δ/rock
NH$_3$	1620 (w)	Rock

Fig. 6. Thermal decomposition of HNO$_3$ (65 wt.%) at 200 °C; (a) intensity measured from mass spectrometer; (b) gas percentages as a function of time.

the bands corresponding to hydroxylammonium and nitrate ions (Fig. 5a), as previously published by Courthéoux et al. [20], in agreement with a full ionized solution.

The Raman spectrum of the collected liquid, issued from the HAN$_{80\%}$–water decomposition at 50 °C using the powdered catalyst (Fig. 5d), displays the characteristic of the nitrate peak at 1040 cm^{-1} accompanied by weak but obvious nitric acid bands at 688, 955 and 1304 cm^{-1}. The absence of the strong hydroxylammonium peak at 1010 cm^{-1} discloses an efficient catalytic activity and the presence of HNO$_3$–NO$_3^-$ mixture is the result of nitric acid formation as decomposition reaction product. On the other hand, the Raman spectra of the collected liquids resulting from the HAN decomposition on the sphere-shaped $3(i + i + i)$rPt catalyst at 50 and 85 °C (Fig. 5b and c), are almost identical with the reactant spectra (HAN$_{80\%}$–water mixture, Fig. 5a). Therefore, only a part of the HAN solution is decomposed by the shaped catalyst.

3.2.2. Stability of nitric acid

As nitric acid has been identified in the condensates, an experiment based on the injection of concentrated nitric acid (65 wt.%) has been performed at 200 °C. Robertson [21] gives a decomposition temperature of gaseous nitric acid between 80 and 475 °C, where nitrogen dioxide formation is evidenced (Eq. (10)):

$$4HNO_3(g) \rightarrow 4NO_2(g) + O_2(g) + 2H_2O(g) \qquad (10)$$
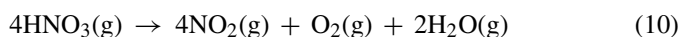
The experimental data lead to the presence of N$_2$ and O$_2$ as major products (Fig. 6a) and only traces of NO and N$_2$O are observed, whereas NO$_2$ is absent. But the intensity of the nitrogen and oxygen peaks varies from one experiment to the other, whereas the O$_2$/N$_2$ mol ratio remains constant (0.24, Fig. 6b), close to the air composition (0.25); therefore, these peaks are only due to air impurities introduced with the reactant through the microsyringe. We can conclude that no decomposition of nitric acid takes part in our conditions at 200 °C; once formed
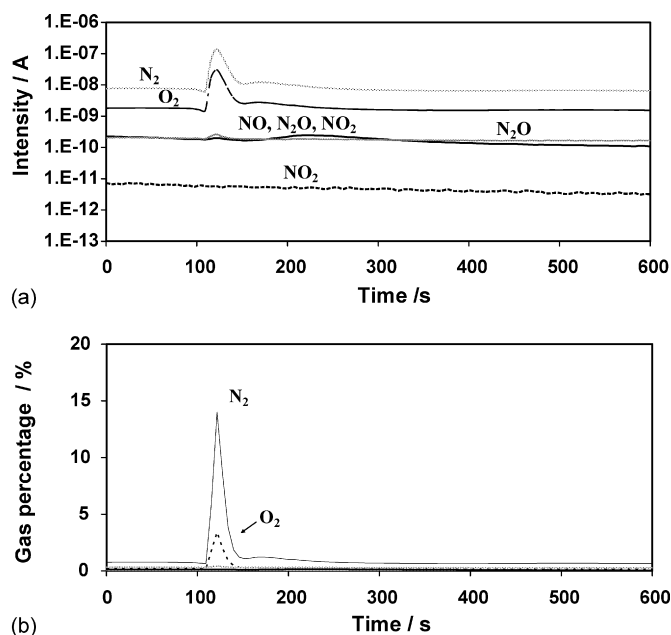
nitric acid molecules remain stable at moderate temperatures and are trapped with water.

It was proposed that the first step of HAN decomposition is the proton exchange leading to the formation of nitric acid and hydroxylamine. But the reaction enthalpy of the corresponding equation (Table 1, Eq. (7)) is very high, more than 160 kJ mol^{-1}, and discards this reaction as a possible first step of the decomposition mechanism. Therefore, the formation of nitric acid is the result of decomposition reactions and not of proton exchange.

3.2.3. Thermal decomposition of HAN solutions

Previous studies have revealed that HAN$_{80\%}$–water mixture decomposes at 120 °C (batch reactor results) [16]; therefore, by setting the reactor temperature at 200 °C, we expect to observe the thermal decomposition in the dynamic reactor. The first detected gaseous species (Fig. 7a) are major nitrogen, nitrogen oxide and minor oxygen, followed by nitrous oxide; only traces of nitrogen dioxide are present. However, the sole NO contribution is difficult to follow from intensity data as the plot corresponding to $m/z = 30$ represents the mixture of NO, NO$_2$ and N$_2$O. Fig. 7b displays the gas percentage variations, calculated from the calibration data. NO content is clearly evidenced as a primary product showing a parallel curve profile as N$_2$, whereas later apparition of N$_2$O and traces of NO$_2$ gases was observed. Oxygen displays a peak intensity of about two orders of magnitude less than nitrogen peak, and a careful examination of the plot shows that the peak maximum is about 5 s before the nitrogen peak maximum (Fig. 7b); this can be explained by the presence of air traces. Therefore, oxygen is not a decomposition product, but only present as impurity.

NO formation can be the result of fast reactions between intermediate products like HONO and HNO as described in literature (Eqs. (11) and (12)) [22]. These species were not detected, the
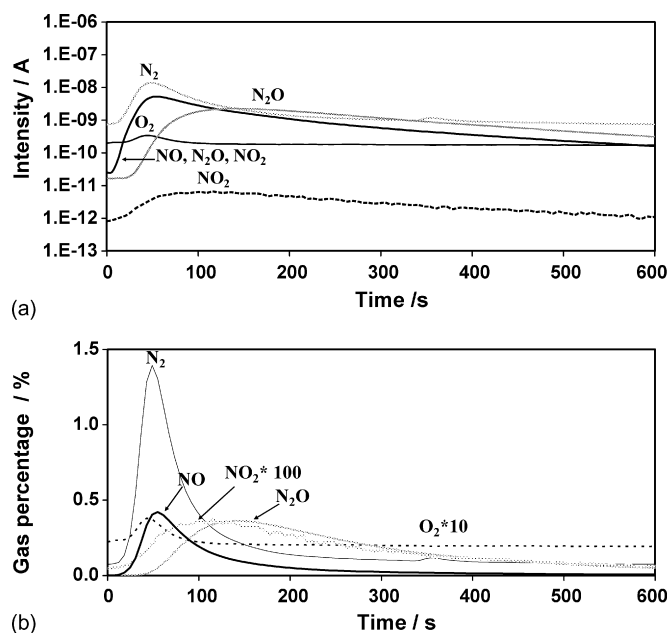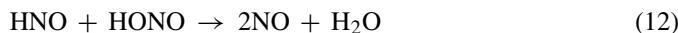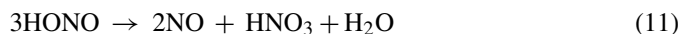
(a)

(b)

Fig. 7. Thermal decomposition of $HAN_{80\%}$–water mixture at 200 °C; (a) intensity measured from mass spectrometer; (b) gas percentages as a function of time.

corresponding intensities at $m/z = 47$ and 31 being embedded into the background noise (intensity $< 10^{-10}$ A).

$$3HONO \rightarrow 2NO + HNO_3 + H_2O \qquad (11)$$

$$HNO + HONO \rightarrow 2NO + H_2O \qquad (12)$$

From Fig. 7b, the estimated N_2:NO:N_2O product molar ratios are 6:2:3. The simultaneous formation of nitrogen and nitric oxide are described as the result of a redox reaction between hydroxylammonium and nitrate ions according to the balanced equation (Eq. (13)):

$$6NH_3OHNO_3(aq)$$
$$= 3N_2(g) + 2NO(g) + 10H_2O(g) + 4HNO_3(g)$$
$$-117.8 \, kJ \, HAN \, mol^{-1} \qquad (13)$$
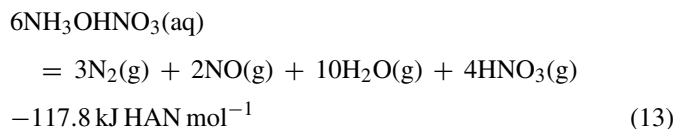
This equation gives a N_2:NO molar ratio of 3:2. The experimental excess of nitrogen can then be explained by the disproportionation of hydroxylammonium cation into ammonium and nitrogen, leading to the formation of ammonium nitrate, according to Eq. (14):

$$6NH_3OHNO_3(aq) = 2N_2(g) + 2NH_4NO_3(s) + 6H_2O(g)$$
$$+ 4HNO_3(g) \quad -653 \, kJ \, mol^{-1} \qquad (14)$$
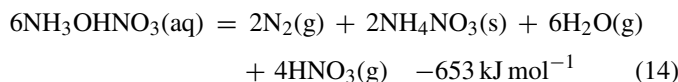
Then, the delayed formation of nitrous oxide is the result of well known decomposition of ammonium nitrate (Eq. (15)):

$$2NH_4NO_3(s) = 2N_2O(g) + 4H_2O(g) \quad -72.9 \, kJ \, mol^{-1}$$
$$(15)$$
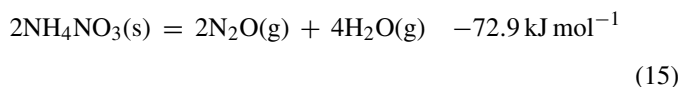
Combining Eqs. (14) and (15) leads to the following decomposition equation (Eq. (16)):

$$6NH_3OHNO_3(aq)$$
$$= 2N_2(g) + 2N_2O(g) + 10H_2O(g) + 4HNO_3(g)$$
$$-121.0 \, kJ \, HAN \, mol^{-1} \qquad (16)$$
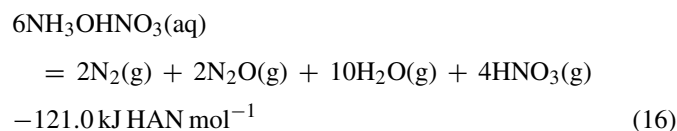
Then, the balanced equation corresponding to the whole thermal decomposition is a linear combination of Eqs. (13) and (16) which satisfies the N_2:NO experimental ratio: $(17) = (13) + 1.5 \times (16)$

$$15NH_3OHNO_3(aq) = 6N_2(g) + 2NO(g) + 3N_2O(g)$$
$$+ 25H_2O(g) + 10HNO_3(g) \qquad (17)$$
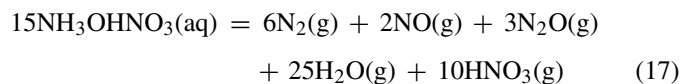
For this equation, the corresponding enthalpy is -119.8 kJ per mol of HAN, a value larger than the data corresponding to the equations presented in Table 1. The experimental amount of N_2O is in rough agreement with the stoichiometric numbers of Eq. (17).

3.2.4. Catalytic decomposition of HAN solution
3.2.4.1. Temperature increase mode. The experiments performed in temperature increase mode lead to the determination of the onset decomposition temperature of the monopropellant for the different catalysts. During the temperature increase mode (Fig. 8a), the injection of HAN (100 μL) on the $5(i + i)$rPt catalyst is carried out at room temperature and then the catalyst containing the HAN solution inside the porosity is heated at a slope of 7 K min^{-1}. The beginning of the decomposition takes place at 77 °C, a value higher than previous results obtained in the static batch reactor under argon (20 °C) [7]; this difference can be explained by the important helium gas flow
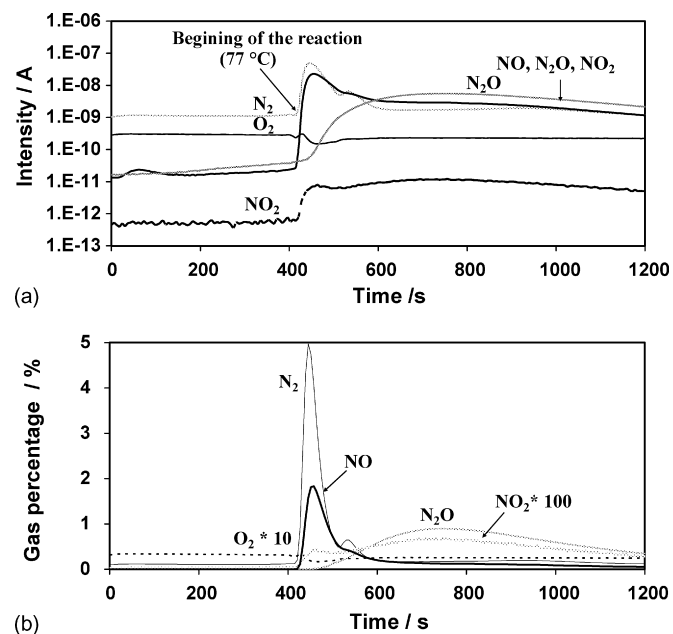

(a)

(b)

Fig. 8. Catalytic decomposition of $HAN_{80\%}$–water mixture with $5(i + i)$rPt catalyst in temperature increase mode; (a) intensity measured from mass spectrometer; (b) gas percentages as a function of time.

(165 mL min^{-1}) which cools locally the sample, thus delaying the decomposition and consequently increasing the decomposition temperature. The typical evolution of the reaction products shows the very fast formation of the primary products N_2 and NO (Fig. 8b); again, oxygen peak is linked to air traces. Then the delayed formation of N_2O, in comparable amounts as NO, and traces of NO_2 are observed with parallel profiles. The experimental molar ratios $N_2:NO:N_2O$ are 5:2:2 which leads to the following balanced equation (Eq. (18)) corresponding to the linear combination (18) = (13) + (16):

$$12NH_3OHNO_3(aq) = 5N_2(g) + 2NO(g) + 2N_2O(g)$$
$$+ 20H_2O(g) + 8HNO_3(g) \qquad (18)$$
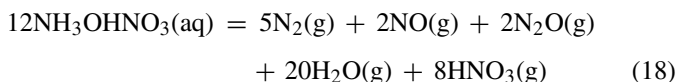
NO and N_2 profiles display a shoulder (Fig. 8a) which can be linked to a second reaction due to residual HAN slipping from the reactor surface.

3.2.4.2. Isothermal mode. These tests have been performed to follow the catalyst activity during 15 successive injections. Firstly, powder and sphere-shaped catalysts have been tested at 50 °C (Fig. 9a and b). The $3(i+i+i)$rPt shaped catalyst has also been tested at a temperature of 85 °C (Fig. 9c), in order to avoid the sphere fragmentation observed previously in the batch reactor [7]. Whatever the catalyst, similar catalytic behaviors are observed; the catalysts remain active during all the injections, displaying mass spectrometer successive peak profiles similar to the temperature peaks observed in the batch reactor [20]. Again, nitrogen and nitric oxide are formed first, followed by nitrous oxide, as in the case of the thermal decomposition. However, some discrepancies can be noted.

The $5(i+i)$rPt powder catalyst leads to a complete and fast HAN decomposition at 50 °C (Fig. 9a) in agreement with the Raman data (Fig. 5d). Therefore, the powder catalytic bed enables a good contact with the propellant solution which can react quantitatively by passing over the active centers. At the same temperature, the sphere-shaped sample displays only an incomplete decomposition with irregular MS peaks (Fig. 9b). A temperature increase to 85 °C leads to more reproducible results (more regular MS peaks), but always incomplete decompositions occur during the successive injections (Fig. 9c).

3.2.4.3. Comparison between thermal and catalytic HAN decompositions. To compare the thermal decomposition and the catalytic reactions on the three catalysts as a function of the successive injections, the gas percentages of N_2, NO and N_2O are presented in Fig. 10a–c. Whatever the gaseous product, the highest observed amounts correspond to the HAN decomposition on the powder $5(i+i)$rPt catalyst: $N_2 = 7\%$, NO = 2%, $N_2O \sim 2\%$ (vol.%, first injection). Only traces of oxygen impurities and nitrogen dioxide are present. For each injection, N_2 and NO appear simultaneously with well-defined MS peaks, whereas N_2O formation is always delayed and displays rounded profiles. We observe a slight decrease of the peak maximum for nitrogen during the successive injections (Fig. 10a) and an important decrease for nitrogen oxide (Fig. 10b), whereas N_2O
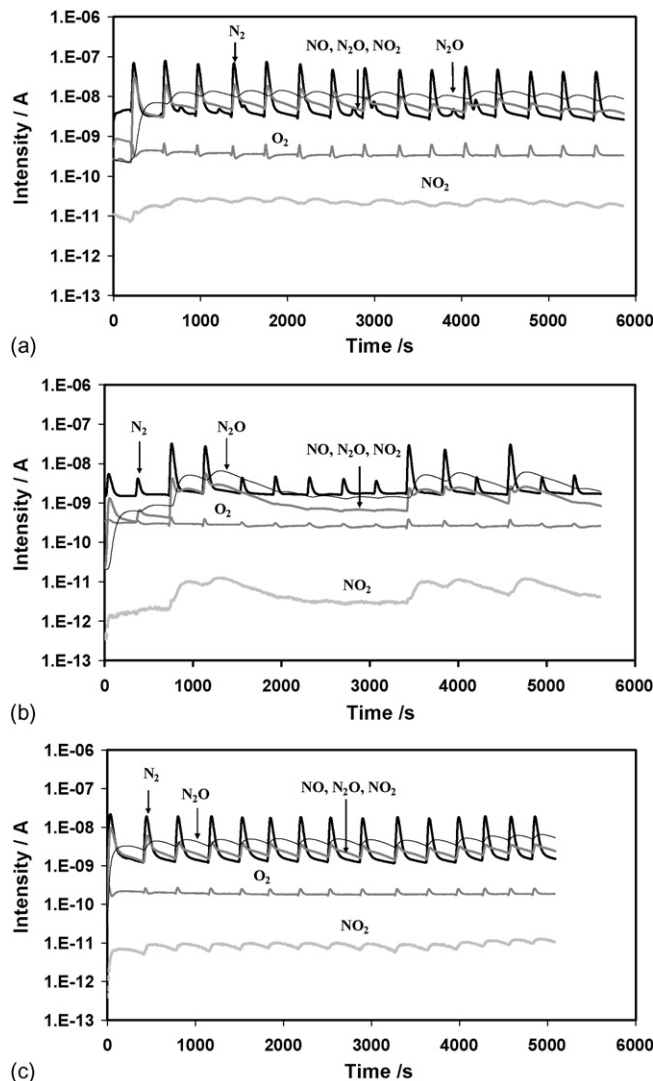

Fig. 9. Peak intensity for catalytic decomposition of HAN solution at 50 °C on powder (a), spheres (b) and at 85 °C on spheres (c).

remains approximately constant (Fig. 10c); these results show a decrease of the catalytic activity, in relation with the intermediate formation of solid ammonium nitrate (Eq. (14)) which can cover a part of the active centers.

The replacement of the powder catalyst by the sphere-shaped $3(i+i+i)$rPt catalyst for the test at 50 °C, leads to a decrease of the gas product percentages by a factor of about 4, by comparison with the previous case: $N_2 = 3\%$, NO = 0.3% and $N_2O \sim 1\%$ (third injection). The major reason is the presence of preferential paths through the catalyst bed, which avoid direct contact between the major part of the propellant and the active centers; this means that the dimensions of the catalytic bed are not optimized for the sphere-shaped catalyst and must be changed for future work by reducing the diameter and increasing the bed length. In this case, the peaks analysis for all injections is not possible due to the activity variation of this catalyst along the test. However, for the 3rd, 4th, 10th, 11th and 13th injections, the gas percentages of the different products are clearly higher. This can be explained by a different path or
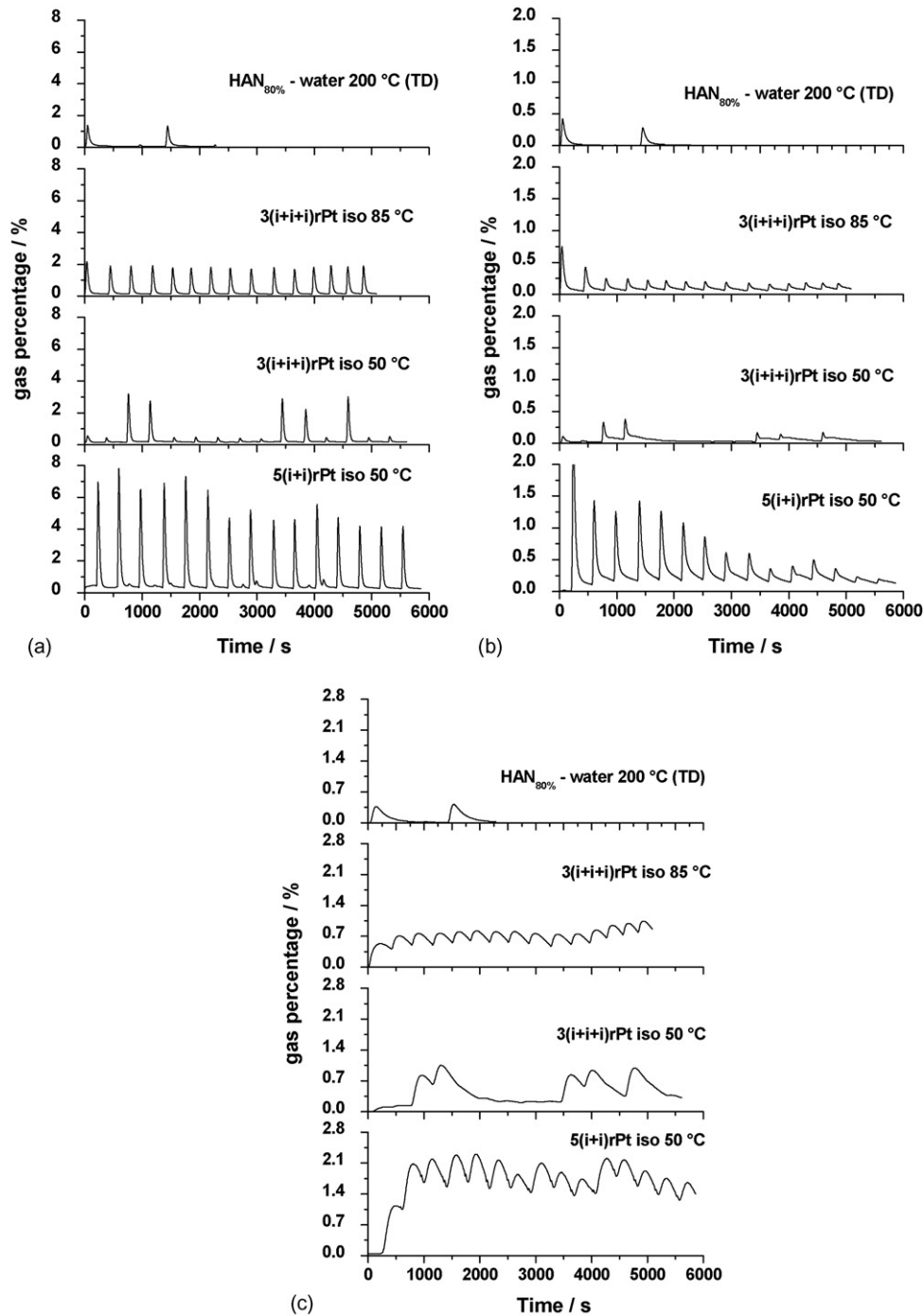
Fig. 10. Gas percentage resulting from catalytic decomposition of $HAN_{80\%}$–water mixture on $5(i+i)$rPt and $3(i+i+i)$rPt catalysts at 50 and 85 °C and from thermal decomposition at 200 °C: (a) N_2; (b) NO; and (c) N_2O for 15 injections.

by a non-reacted solution accumulation during the injections which penetrates into the spheres porosity. Another important characteristic is that no sphere fragmentation was observed, due to the large amount of non-reacted HAN solution which limits the heat release due to the propellant decomposition. However, the selectivity of the reaction into kinetic products is independent of the support shape.

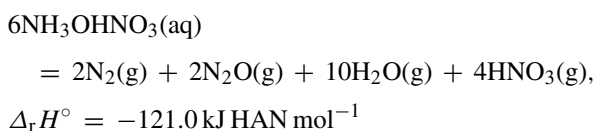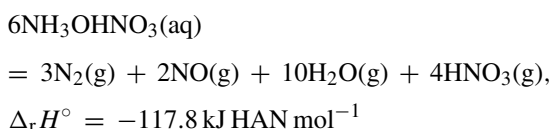The tests performed at 85 °C with the same catalyst are more regular and reproducible than at 50 °C. Nevertheless the catalytic activity remains low by comparison with the powder sample and the catalyst was not fragmented after the tests, in agreement with the preferential path explanation.

For the thermal decomposition at 200 °C, only two injections have been carried out. The gas percentage of the different products are of the same order of magnitude as the values obtained with the sphere-shaped catalyst at 85 °C, displaying thus that the decomposition is only partial despite the higher reaction temperature.

4. Conclusion

A dynamic reactor with mass spectroscopy online product analysis has been used to study the thermal and catalytic decomposition of ionic liquid HAN-based monopropellants. The activity of different catalysts has been evaluated, by determining qualitatively and quantitatively the reaction products. A careful calibration of the expected products detected by the mass spectrometer (N_2, O_2, N_2O, NO and NO_2) has been performed. The analytical results have been supplemented by Raman spectroscopy of the aqueous solutions trapped after the reactor.

The thermal and catalytic decomposition of HAN (80 wt.%)–water mixture gave primary products (major N_2, medium NO) and secondary products (medium N_2O and traces NO_2). From the data, a reaction mass balance could be proposed, based on the combination of two parallel competitive reactions:

$$6NH_3OHNO_3(aq)$$

$$= 3N_2(g) + 2NO(g) + 10H_2O(g) + 4HNO_3(g),$$

$$\Delta_r H^\circ = -117.8\,kJ\,HAN\,mol^{-1}$$

$$6NH_3OHNO_3(aq)$$

$$= 2N_2(g) + 2N_2O(g) + 10H_2O(g) + 4HNO_3(g),$$

$$\Delta_r H^\circ = -121.0\,kJ\,HAN\,mol^{-1}$$

The influence of the catalyst shape (powder or spheres) has been followed. The isothermal tests at $50\,^\circ C$ display the best activity for the powder catalyst with a complete decomposition of the HAN solution, due to a good contact between catalyst bed and monopropellant. On the other hand, the sphere-shaped catalyst leads only to a partial HAN decomposition, due to preferential paths through the catalyst bed. The thermal decomposition at $200\,^\circ C$, leads also to a partial reaction.

In order to improve the dynamic reactor performances, the catalytic bed dimensions have to be changed as well as the physical state of the monopropellant mixture by using a gel or developing a spray injection system. The comparison of the sphere-shaped catalyst with laboratory shaped samples is currently under progress.

Acknowledgements

References

[1] V. Bombelli, D. Simon, J. Moerel, T. Marée, Economic benefits of the use of non-toxic mono-propellants for spacecraft applications, AIAA Papers (2003) 4783.

[2] L. Courthéoux, D. Amariei, S. Rossignol, C. Kappenstein, N. Pillet, M. Ford, Thermal and catalytic decomposition of HNF and HAN-based propellants, European Space Agency, Space Propul. SP-557 (2004) 106–111 (special publication).

[3] R. Eloirdi, S. Rossignol, C. Kappenstein, D. Duprez, N. Pillet, Design and use of a batch reactor for catalytic decomposition of propellants, J. Propul. Power 19 (2003) 213–219.

[4] R. Eloirdi, S. Rossignol, C. Kappenstein, D. Duprez, N. Pillet, Catalytic decomposition of different monopropellants, European Space Agency, Space Propul. SP-465 (2000) 263–270 (special publication).

[5] L. Courthéoux, R. Eloirdi, S. Rossignol, C. Kappenstein, D. Duprez, N. Pillet, Catalytic decomposition of HAN–water binary mixtures, AIAA Papers (2002) 4027.

[6] L. Courthéoux, S. Rossignol, C. Kappenstein, D. Duprez, N. Pillet, Improvement of catalyst for the decomposition of HAN-based monopropellant—comparison between aerogel and xerogel, AIAA Papers (2003) 4645.

[7] L. Courthéoux, D. Amariei, S. Rossignol, C. Kappenstein, Facile catalytic decomposition at low temperature of energetic ionic liquid as hydrazine substitute, Eur. J. Inorg. Chem. (2005) 2293–2295.

[8] L. Courthéoux, E. Gautron, S. Rossignol, C. Kappenstein, Transformation of supported platinum on silicon doped alumina during the catalytic decomposition of energetic ionic liquid, J. Catal. 232 (2005) 10–18.

[9] Y. Batonneau, L. Courthéoux, P. Esteves, L. Pirault-Roy, S. Rossignol, C. Kappenstein, N. Pillet, Design and development of a dynamic reactor with online analysis for the catalytic decomposition of monopropellants, AIAA Papers (2004) 3835.

[10] J.W. Schoppelrei, T.B. Brill, Spectroscopy of hydrothermal reactions. 7 Kinetics of Aqueous [NH₃OH]NO₃ at 463–523 K and 27.5 MPa by infrared spectroscopy, J. Phys. Chem. A 101 (1997) 8593–8596.

[11] D. Zube, S. Christofferson, E. Wucherer, B. Reed, Evaluation of HAN-based propellant blends, AIAA Papers (2003) 4643.

[12] Y.P. Chang, K.K. Kuo, Assessment of combustion characteristics and mechanism of hydroxylammonium nitrate-based liquid monopropellant, J. Propul. Power 18 (2002) 1076–1085.

[13] Y.P. Chang, E.K. Boyer, K.K. Kuo, Combustion behaviour and flame structure of XM46 liquid propellant, J. Propul. Power 17 (2001) 800–808.

[14] A. Roine, HSC Chemistry® for Windows, Chemical reaction and equilibrium software with extensive thermochemical database, Version 5.1, Outokumpu Research Oy, Pori, Finland, 2002, ISBN 952-9507-08-9, http://www.outokumpu.com/hsc.

[15] NIST Chemistry WebBook http://webbook.nist.gov/chemistry/.

[16] L. Courthéoux, E. Gautron, S. Rossignol, C. Kappenstein, Platinum supported on doped alumina catalysts for propulsion applications. Xerogels versus aerogels, J. Non-Cryst. Solids 350 (2004) 113–119.

[17] F. Popa, L. Courthéoux, E. Gautron, S. Rossignol, C. Kappenstein, Aerogel and xerogel catalysts based on θ-alumina doped with silicon for high temperature reactions, Eur. J. Inorg. Chem. 3 (2005) 543–544.

[18] M.M. Decker, N. Klein, E. Freedman, C.S. Leveritt, J.Q. Wojciechowsk, HAN (hydroxylammonium nitrate)-based liquid propellants: physical properties, Army Ballist. Res. Lab., Report BRL-TR, 1987, p. 2864.

[19] N. Minogue, E. Riordan, J.R. Sodeau, Raman spectroscopy as a probe of low-temperature ionic speciation in nitric and sulfuric acid stratospheric mimic systems, J. Phys. Chem. A 107 (2003) 4436–4444.

[20] L. Courthéoux, D. Amariei, S. Rossignol, C. Kappenstein, Thermal and catalytic decomposition of HNF and HAN liquid ionic as propellants, Appl. Catal. B 62 (2005) 217–225.

[21] G.D. Robertson Jr., Ph.D., California Institute of Technology Pasadena, California, 1953.

[22] H. Lee, T. Litzinger, Chemical study of HAN decomposition, Combust. Flame 135 (2003) 151–169.